machines

MDPI

Article

Laser Directed Energy Deposition-Based Additive Manufacturing of Fe20Cr5.5AlY from Single Tracks to Bulk Structures: Statistical Analysis, Process Optimization, and Characterization

Jinoop Arackal Narayanan [1,2,*], Farzaneh Kaji [1,2], Mark Zimny [2] and Ehsan Toyserkani [1]

[1] Multi-Scale Additive Manufacturing Lab, Department of Mechanical and Mechatronics Engineering, University of Waterloo, Waterloo, ON N2L 3G1, Canada
[2] Promation, 2767 Brighton Rd., Oakville, ON L6H 6J4, Canada
* Correspondence: janarayanan@uwaterloo.ca

Abstract: Laser directed energy deposition (LDED) can be deployed for depositing high-performance materials for various engineering applications. Alumina-forming steel is a high-performance material that possesses excellent corrosion and oxidation resistance, finding application in the power generation sector. In the present work, LDED using powder feeding (LDED-PF) was used to deposit Fe20Cr5.5AlY alloy using single-track, multi-track, and multi-layer deposition on SS 316L substrate. Response surface methodology (RSM)-based optimization was used to optimize the single-track deposition. The relationship between the track geometry parameters and the build rate with the LDED-PF processing parameters was studied. Further, the nonlinear relationship among the major process parameters was developed and an analysis of variance (ANOVA) was utilized to find significant parameters. The multi-track deposition yielded densely clad layers with a columnar grain structure. The presence of complex oxide slag of Y, Al, and Zr on the clad layer was detected. A micro-hardness of 240–285 HV was observed in the clad layer, with a hardness of 1088–1276 HV at the slag layer. The multi-layered structures showed a relative density of 99.7% with columnar growth and an average microhardness of 242 HV. The study paves the way for the deposition of dense alumina-forming steel structures for building components for power generation applications.

Keywords: laser directed energy deposition; cladding; Fe–Cr–Al alloys; process optimization; characterization; bulk components

Citation: Arackal Narayanan, J.; Kaji, F.; Zimny, M.; Toyserkani, E. Laser Directed Energy Deposition-Based Additive Manufacturing of Fe20Cr5.5AlY from Single Tracks to Bulk Structures: Statistical Analysis, Process Optimization, and Characterization. *Machines* **2023**, *11*, 58. https://doi.org/10.3390/machines11010058

Academic Editors: Shiva Sekar and Sunil Pathak

Received: 1 December 2022
Revised: 31 December 2022
Accepted: 3 January 2023
Published: 4 January 2023

1. Introduction

The transition to sustainable power generation is progressing briskly across the globe, increasing interest in biomass combustion [1]. The deployment of biomass in fossil fuel results in the generation of a hostile combustion environment, leading to the corrosion of boiler components and a reduction in operational efficiency [2]. In addition, the catastrophic breakdown of power plants is created by the corrosion of boiler pipes running in high-temperature environments. One of the methods to prevent hostile elevated temperature corrosion conditions inside boilers is to employ corrosion-resistant materials. However, corrosion-resistant materials are generally expensive, and it is not economically possible to substitute conventional ferritic steels. Presently, ferritic steels are used for manufacturing heat exchanger components, and nickel-based alloys are generally used for corrosion resistance as they form chromia layers on the surface [3]. One of the alternatives is the iron-based alloys (FeCr, FeAl, Fe–Cr–Al, etc.) due to the lower cost of the alloy as compared to other thermal barrier coatings and the availability of iron. The alloy possesses good mechanical properties, oxidation, and corrosion resistance characteristics, which increase their deployment in automotive, marine, and power generation sectors [4,5].

Fe–Cr–Al alloys are Fe-based ferritic materials having Cr and Al, with some containing 2–3% molybdenum (Mo). The major reason for the excellent surface properties of the alloy is its capability to create a thin, slow-growing, tenacious, and adherent α-alumina (α-Al_2O_3) oxide scale on its surfaces, which guards the alloys against additional degradation [6]. The surface protection of the Fe–Cr–Al alloys begins with the growth of weakly protective outward-growing transient Al_2O_3 phases (δ-Al_2O_3, θ-Al_2O_3, and γ-Al_2O_3), which start growing at temperatures below 900 °C. These transient phases are converted to stable α-Al_2O_3 phases over time [7–9]. At the same time, the α-Al_2O_3 growth is dominated in the initial phases of oxidation at higher temperatures (T > 1000 °C) [10]. The presence of Cr permits the α-Al_2O_3 with a lower content of Al due to the formation of Cr_2O_3 that acts as an easy nucleation site for α-Al_2O_3 [10–12]. The alloy also has a small quantity of reactive elements, such as Y, Hf, Zr, and Ce, to improve the adhesion of the oxide scale during cyclic oxidation conditions. It also allows the slow growth of the oxide scale. The oxides of these elements also aid to improve the creep resistance of the alloy through dispersion strengthening.

Generally, Fe–Cr–Al alloy components are produced using casting and deformation methods, such as hot rolling and powder metallurgy. However, the manufacturing of complex-shaped components with these processes is difficult due to their inherent limitations [6]. In addition, several techniques are reported in the literature, such as spraying techniques (based on arc [13], plasma [14], etc.), and laser cladding [15] for Fe–Cr–Al coating. Additionally, welding techniques, such as gas-tungsten arc welding (GTAW), tungsten inert gas welding (TIG), and laser welding, are deployed for depositing Fe–Cr–Al weld overlays. Among the different techniques, laser cladding can yield dense coatings with a fine microstructure, controlled dilution, and good metallurgical bonding with the substrate [16,17]. On the process side, laser cladding is a subset of laser directed energy deposition (LDED)-based additive manufacturing (AM). LDED permits the manufacturing of complex-shaped metallic components and the deposition of materials by using a laser source and dynamically fed feedstock material. The laser source is used to create a melt pool on the substrate for depositing the first layer, and the feedstock material is added to the developed melt pool. This permits the material deposition as per the trajectories generated from the digital model data. For building multi-layer structures, the materials are added to the melt pool formed on the previously built layer followed by a layer-by-layer deposition, which leads to the fabrication of 3D components [18,19]. LDED can be classified into LDED using wire feeding (LDE-WF) and LDED using powder feeding (LDED-PF). LDED-PF is widely used for its ability to build components with fine features and controlled laser energy density [20].

Researchers have attempted laser cladding of an Fe–Cr–Al alloy using LDED and its characterization. Liu et al. [21] deposited Fe-24.5Cr-4Al-0.56Y layers with constant process parameters by using a pre-placed layer of powder on the substrate and investigated the microstructure, build quality, and oxidation resistance. The deposited layer revealed micro-cracks, and excellent oxidation properties were observed at a temperature range of 1000–1200 °C. Nagarathnam and Komvopoulos [22] studied the LDED-PF of pre-mixed Fe–Cr–Al-Y and studied the effect of process parameters (laser power and scanning speed at a constant powder feed rate) on the microstructure, hardness, and oxidation behavior. The deposited layers exhibited a fine grain structure with a hardness of 409 kg/mm^2, and excellent oxidation resistance. Hot corrosion studies on LDED-PF- and LDED-WF-deposited Fe–Cr–Al alloys were reported by Yang et al. [23] and Reddy et al. [1], respectively. Yang et al. [23] used pre-mixed Fe, Cr, Al, and Si powders to deposit the Fe-22Cr-5Al-2Si material with constant process parameters, and continuous hot corrosion tests were completed in a salt solution of Na_2SO_4 and K_2SO_4 at 800 °C in air. Meanwhile, Reddy et al. [1] used wire-based laser cladding of Kanthal APMT™ (an Fe–Cr–Al–Mo alloy) with constant process parameters for studying the effects of HCl and KCl on Fe–Cr–Al-clad layers at 450 °C.

The above studies focused on the effect of laser cladding on the corrosion behavior, oxidation behavior, and microstructural analyses with constant process parameters without providing information on process optimization. The literature review also indicates that there is a lack of systematic parametric studies and process optimization on the LDED-PF of Fe–Cr–Al–Y pre-alloyed powder. Thus, there is a need to develop the process for LDED-PF of Fe–Cr–Al–Y pre-alloyed powder with a maximum build rate and desired dilution to build high-quality cladding and engineering components.

The present research reports the effect of LDED-PF process parameters on the track geometry (width, height), dilution, and build rate. Subsequently, multi-objective optimization is performed to select optimal process parameters yielding a high build rate and target dilution. The study is further extended to the development and characterization of multi-track clad layers and multi-layered bulk structures. The understandings from the above investigations will be used to build large-area claddings and engineering components from Fe20Cr5.5AlY alloy using LDED-PF.

2. Materials and Methods

2.1. Materials

Gas-atomized Fe20Cr5.5AlY alloy powder with particle sizes ranging from 15 to 45 µm was procured from M/s Sandvik. The d10, d50, and d90 of the powder particles were 16.3 µm, 28.1 µm, and 48.4 µm, respectively. The powder has a spherical morphology with satellite particles as shown in Figure 1. The satellite particles are formed due to the faster solidification rates of smaller particles, which are adhered during atomization to the surface of the large particles. The chemical composition of the powder as provided by the supplier is given in Table 1. SS316L substrate is used as the base material for LDED-PF. Figure 1c presents the element spectrum of the powder obtained using energy dispersive spectroscopy (EDS) analysis. SS316L substrate is used as the base material for LDED-PF.

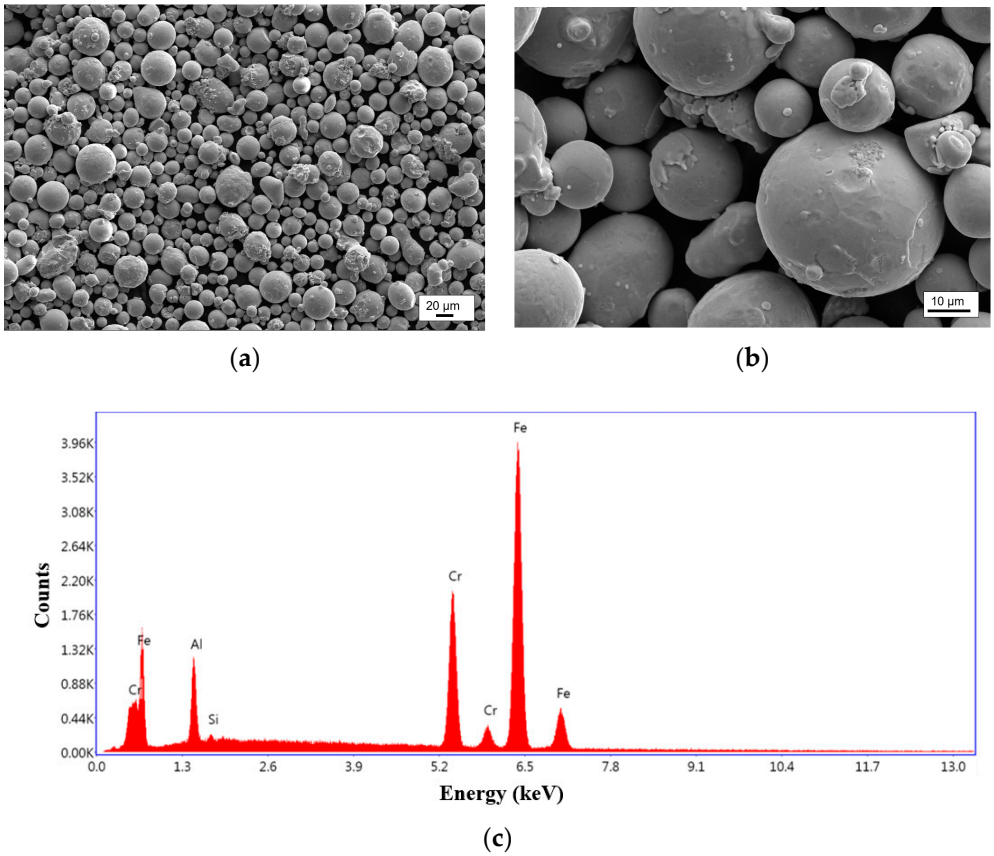

(**a**) (**b**)

(**c**)

Figure 1. Fe20Cr5.5AlY powder used for LDED-PF (**a**) morphology at low magnification, and (**b**) morphology at higher magnification; (**c**) element spectrum.

Table 1. Chemical composition of the powder.

Element	Weight Percentage (%)
Cr	20.6
Al	5.3
Si	0.34
Hf	0.18
Mn	0.16
Ni	0.10
N	0.05
Zr	0.04
Y	0.03
C	0.01
Fe	Balance

2.2. LDED-PF of Fe20Cr5.5AlY

Figure 2 presents the schematic of the LDED-PF system developed in-house and used for the deposition. The system essentially consists of IPG photonics make 1 kW continuous wave fiber laser; GTV make dual hopper powder feeder; Fraunhofer make coaxial deposition. A 6-axis Fanuc robotic arm and a 2-axis positioner are used for motion planning during the LDED-PF process. An operating system developed in-house is deployed to control the robotic system and the auxiliary components. PROERA 3D, a CAD/CAM software developed in-house is used for the tool path generation. Argon gas at a flow rate of 10 L per minute is used as shielding gas and carrier gas. A laser spot diameter of 1.2 mm at the substrate surface is used for the deposition [24,25].

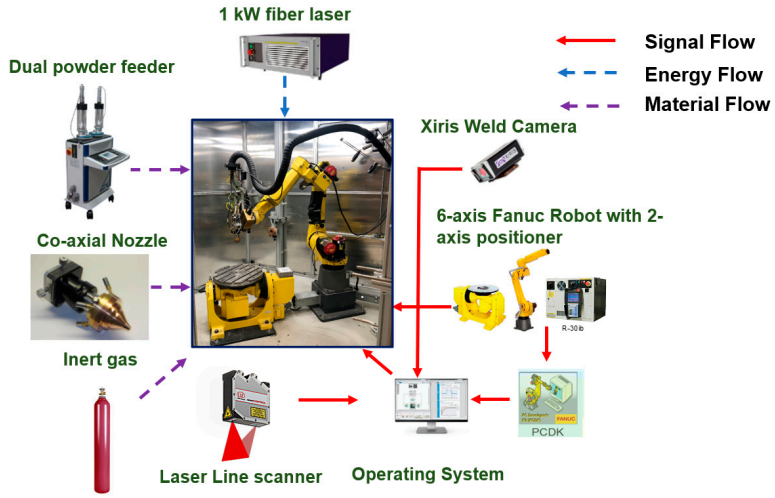

Figure 2. Schematic of LDED-PF system used for deposition.

Prior to the experiment, the laser power (P), scanning speed (V), and powder feed rate (F) were preliminarily analyzed by single-factor tests. It was observed that the track quality deteriorated significantly in terms of continuity, surface oxidation, and bonding with the substrate at $P < 600$ W and with F and V higher than 8 g/min and 11 mm/s, respectively. Based on the above, the range of process parameters for the design of experiments is selected. The process parameters and their levels selected for the design of experiments are provided in Table 2. Central composite design (CCD) methodology was used for the design of experiments, with the central point experiments repeated three times.

Table 2. Process parameters and levels.

Parameter	Code Levels		
	−1	**0**	**+1**
P (W)	600	700	800
V (mm/s)	7	9	11
F (g/min)	4	6	8

Response surface methodology (RSM), a well-recognized and powerful approach, was used to study the relationship between the LDED-PF process parameters and output responses. RSM is a comprehensive optimization method used to examine and optimize the effect of two or more factors on quality criteria. Compared with other experimental methods, RSM can provide a perfect correlation between the output and input factors with fewer experimental trials, while retaining high modelling accuracy [26,27].

2.3. Characterization

Single-tracks, multi-track clad layers, and multi-layered depositions are sectioned using water jet machining. The cut specimen is sectioned using a precision cutter, cold-mounted, and polished using an automatic polisher (Make: Metlab; Model: Metpol-A). The samples are electrochemically etched using an oxalic acid solution at 20 V for 5–10 s. Cross-sections of the single-track, multi-track clad layers and multi-layer structures are examined using a digital microscope (Make: Keyence; Model: VHX-7000) in polished and etched conditions. Microhardness measurements are taken using a Vickers automated hardness tester (Make: CLEMEX; Model: CMT) by applying a load of 300 gm for a dwell period of 15 s. Scanning electron microscope (SEM) (Make: Tescan, Model: VEGA3) with EDS (Make: Bruker, Model: Quantax) was used to analyze the composition of the samples. The density of the multi-layered samples (ρ) was measured using the Archimedes density analyzer (Make: GAOTEK; Model: GT00WI00ZV) using Equation (1).

$$\rho = \frac{W_D \rho_w}{W_D - W_w} \tag{1}$$

where W_D, W_w and ρ_w are the dry weight, wet weight, and density of distilled water, respectively. The density of each sample was measured three times to obtain the average density. The reference material used for evaluating the relative density is 7.10 g/cc [28].

3. Results and Discussion

3.1. Effect of Process Parameters

3.1.1. Track Width

Track width (W) is a function of the LDED-PF process parameters. In order to understand the effect of LDED-PF process parameters on W, an experimental analysis is carried out using two combined parameters: laser energy per unit length (LEL) and powder feed per unit length (PFL). LEL is defined as the ratio between P and V (Equation (2)), while PFL is the ratio between F and V (Equation (3)) [19]. Figure 3 presents the effect of LEL and PFL on W.

$$\text{Laser Energy per unit Length (LEL)} = \frac{Laser\ Power}{Scan\ speed} = \frac{P}{V} \tag{2}$$

$$\text{Powder Feed per unit Length (PFL)} = \frac{Powder\ Feed\ Rate}{Scan\ Speed} = \frac{F}{V} \tag{3}$$

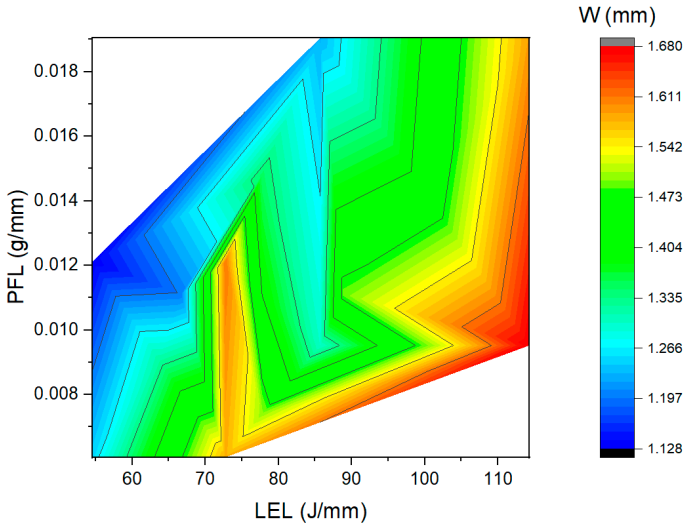

Figure 3. Effect of LEL and PFL on *W*.

W increases with an increase in LEL as shown in Figure 3. A positive relation between *W* and LEL is mainly due to the increase in the laser irradiation energy with an increase in LEL, which leads to a higher melt pool temperature. During LDED-PF, the center of the melt pool will be at a higher temperature than the edges [29], which might be due to the Gaussian heat distribution and additional heat transfer at the edges. The difference in the temperature inside the melt pool leads to variations in the thermophysical properties within the melt pool. The major factors governing the melt pool dynamics are the surface tension gradient and the variation in viscous forces inside the melt pool. The Marangoni effect results in the mass transfer inside the melt pool as fluid moves from the region with a lower surface tension to the region with a higher surface tension. The Marangoni flow inside the melt pool is primarily dependent on the surface tension gradient ($d\gamma/dT$) within the melt pool [30]. A negative $d\gamma/dT$ results in a reduction in surface tension with an increase in the temperature, which allows for outward melt pool flow. This results in the formation of a wider melt pool with an increase in LEL during LDED-PF. At the same time, an increase in PFL leads to the availability of more powder for deposition, leading to an increased track width. However, the effect of LEL is more significant as compared to that of PFL.

An analysis of variance (ANOVA) of the experimentally obtained data is performed to statistically examine the relative significance of the LDED-PF process parameters on the response variables. Table 3 presents the ANOVA of the track width. In Table 3, the columns SS and DF represent the sum of squares and degrees of freedom, respectively. The ratio between SS and corresponding DF drives the MS, and the *F* value is obtained from the ratio between the MS of each effect and the MS corresponding to the residual. The *p*-value indicates the significance of the process parameter on the response. Any control parameter having a $p < 0.05$ would have a significant impact on the selected response attribute [31]. *P* is the most significant process parameter influencing *W* and the contribution of *P* towards *W* is 84.6%. The Pareto chart presented in Figure 4 also shows that *P* is the most significant parameter in determining the *W* of Fe20Cr5.5AlY deposits. The response model of the *W* is shown in Equation (4). The R^2 of 0.96 indicates a good correlation between the experimental values and predicted values and a *p* value < 0.05 for the model indicates its significance. It can be concluded that the model is significant with a 94.8% contribution towards explaining the behavior of *W*.

$$W = 0.45 + 0.00432\,P - 0.071\,V - 0.2509\,F - 0.000002\,P \times P + 0.00069\,V \times V + 0.01307\,F \times F + 0.000041\,P \times V + 0.000078\,P \times F + 0.00213\,V \times F \quad (4)$$

Table 3. ANOVA analysis of *W*.

Source	DF	Adj SS	Adj MS	*F*-Value	*p*-Value
Model	9	0.376492	0.041832	23.36	0.000
Linear	3	0.364450	0.121483	67.83	0.000
P	1	0.335256	0.335256	187.19	0.000
V	1	0.011972	0.011972	6.68	0.032
F	1	0.017223	0.017223	9.62	0.015
Square	3	0.008997	0.002999	1.67	0.249
$P \times P$	1	0.001527	0.001527	0.85	0.383
$V \times V$	1	0.000021	0.000021	0.01	0.917
$F \times F$	1	0.007401	0.007401	4.13	0.077
Two-Way Interaction	3	0.003045	0.001015	0.57	0.652
$P \times V$	1	0.000545	0.000545	0.30	0.596
$P \times F$	1	0.001922	0.001922	1.07	0.331
$V \times F$	1	0.000578	0.000578	0.32	0.586
Error	8	0.014328	0.001791		
Lack-of-Fit	5	0.013970	0.002794	23.41	0.013
Pure Error	3	0.000358	0.000119		
Total	17	0.390820			

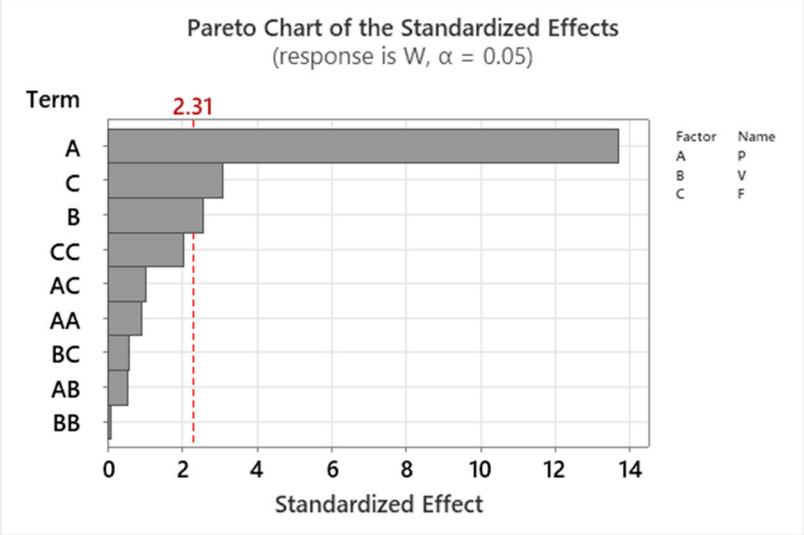

Figure 4. Pareto chart (significance level, $\alpha = 0.05$) of the standardized effects of process parameters on *W*.

3.1.2. Track Height

Figure 5 presents the variation in *H* as a function of LEL and PFL. As the LEL increases, the energy available for melting the fed powder particle and substrate increases, which further increases the catchment efficiency of the deposition and available energy in the melt pool. Catchment efficiency is defined as the ratio between the amount of material deposited to the amount of material fed to the melt pool for deposition. With an increase in the catchment efficiency, a greater amount of powder particles will be melted and deposited. The increase in LEL is also a function of the reduction in *V*. As *V* decreases, the interaction time between the laser beam and powder particle/substrate increases. The interaction time is defined as the ratio between the beam diameter and *V*. An increase in the interaction time increases the amount of powder captured by the melt pool and the availability of a greater amount of energy in the melt pool, which increases the deposit height. As *V* decreases and *F* increases, the PFL increases, which shows that a greater amount of powder is available for deposition. It can also be noted from Figure 5 that the effect of PFL is more significant as compared to that of LEL, which shows that amount of powder available per unit length has more of an effect on *H*.

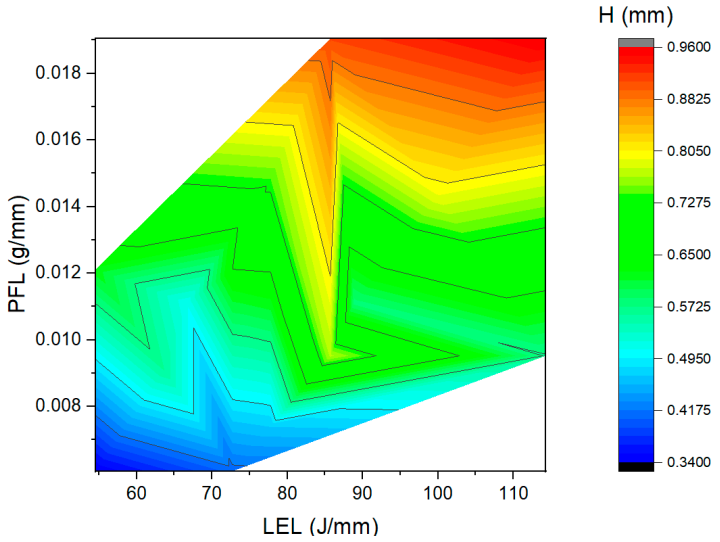

Figure 5. Effect of LEL and PFL on *H*.

An ANOVA is performed to statistically examine the relative significance of the LDED-PF process parameters on *H* as presented in Table 4. *V* and *F* are the most significant process parameters influencing the track height, while *P* has a lower effect. The contributions of *V* and *F* towards *H* are 47.6% and 40%, respectively. The Pareto chart presented in Figure 6 also shows that *V* and *F* are the most significant parameters in determining the *H* of the Fe20Cr5.5AlY deposits. The response model of the *H* is shown in Equation (5). The R^2 of 0.96 indicates a good correlation between the experimental values and predicted values, and the model's significance is indicated by the *p* value < 0.05. It can be concluded that the model is significant with a 97.6% contribution towards explaining the behavior of *H*.

$$H = 1.74 + 0.00446\,P - 0.536\,V - 0.055\,F - 0.000005\,P \times P + 0.01980\,V \times V + 0.00268\,F \times F + 0.000161\,P \times V + 0.000134\,P \times F - 0.00059\,V \times F \quad (5)$$

Table 4. ANOVA analysis of *H*.

Source	DF	Adj SS	Adj MS	*F*-Value	*p*-Value
Model	9	0.412403	0.045823	21.91	0.000
Linear	3	0.376645	0.125548	60.03	0.000
P	1	0.000029	0.000029	0.01	0.909
V	1	0.200789	0.200789	96.01	0.000
F	1	0.175828	0.175828	84.07	0.000
Square	3	0.021678	0.007226	3.46	0.071
$P \times P$	1	0.006191	0.006191	2.96	0.124
$V \times V$	1	0.016998	0.016998	8.13	0.021
$F \times F$	1	0.000310	0.000310	0.15	0.710
Two-Way Interaction	3	0.014079	0.004693	2.24	0.160
$P \times V$	1	0.008256	0.008256	3.95	0.082
$P \times F$	1	0.005778	0.005778	2.76	0.135
$V \times F$	1	0.000045	0.000045	0.02	0.887
Error	8	0.016731	0.002091		
Lack-of-Fit	5	0.016227	0.003245	19.29	0.017
Pure Error	3	0.000505	0.000168		
Total	17	0.429135			

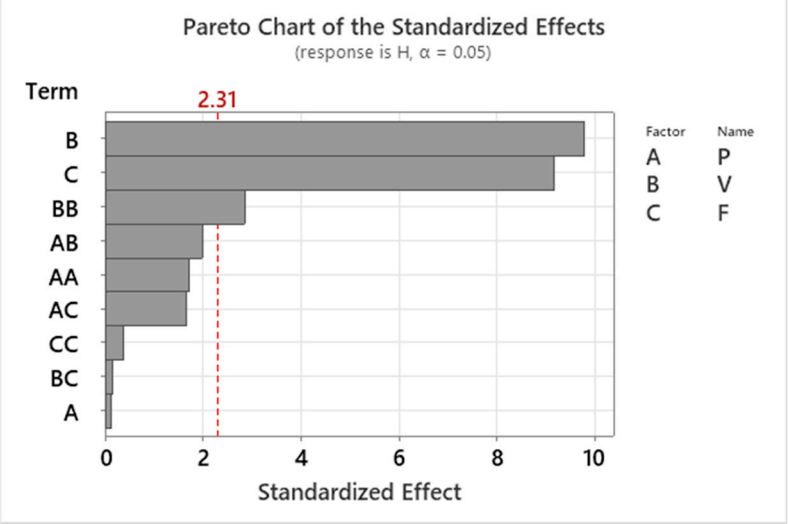

Figure 6. Pareto chart (significance level, $\alpha = 0.05$) of the standardized effects of process parameters on *H*.

3.1.3. Build Rate

The build rate (*BR*) is defined as the product of the track area and *V*. As seen in Figure 7, the *BR* increases with an increase in LEL and PFL. This is mainly due to the increase in *W* and *H* with an increase in LEL and PFL due to an increase in the amount of energy and powder available for deposition, respectively. However, the effect of PFL is found to be more significant as compared to that of LEL. This is mainly due to the higher influence of *F* on the amount of material available for deposition or the track area. Further, *V* governs how fast the deposition head moves to add materials during LDED-PF. A lower *V* can increase the track area due to higher values of *W* and *H*, while it decreases the speed at which the deposition is happening. On the other hand, a higher *V* increases the deposition speed and reduces the track area. An increase in the *BR* at the central region of the plot (refer to Figure 7) can be due to the above-mentioned effect of *V* on the *BR*.

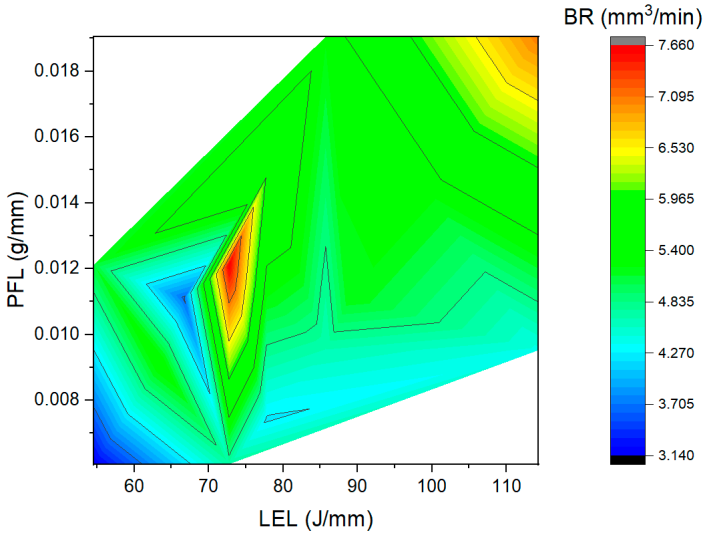

Figure 7. Effect of LEL and PFL on *BR*.

ANOVA is performed to statistically examine the relative significance of the LDED-PF process parameters on the *BR* as presented in Table 5. *F* is the most significant process parameter influencing the *BR*, followed by *P* and *V*. The contribution of *F* towards the *BR* is 51%. The Pareto chart presented in Figure 8 also shows that *F* is the most significant

parameter in determining the *BR* of the Fe20Cr5.5AlY deposits. The response model of the *BR* is shown in Equation (6). The R^2 of 0.97 indicates a good correlation between the experimental values and predicted values and the model's significance is indicated by the *p* value < 0.05. It can be concluded that the model is significant with a 97.32% contribution towards explaining the behavior of the *BR*.

$$BR = 5.83 + 0.0457\,P - 3.324\,V - 1.896\,F - 0.000046\,P \times P + 0.1048\,V \times V + 0.0490\,F \times F + 0.001559\,P \times V + 0.001895\,P \times F + 0.0526\,V \times F \quad (6)$$

Table 5. ANOVA analysis of *BR*.

Source	DF	Adj SS	Adj MS	*F*-Value	*p*-Value
Model	9	18.2006	2.02229	30.83	0.000
Linear	3	15.0137	5.00457	76.29	0.000
P	1	5.3092	5.30915	80.93	0.000
V	1	0.0366	0.03655	0.56	0.477
F	1	9.6680	9.66801	147.38	0.000
Square	3	0.9055	0.30185	4.60	0.037
$P \times P$	1	0.5625	0.56250	8.57	0.019
$V \times V$	1	0.4761	0.47609	7.26	0.027
$F \times F$	1	0.1040	0.10403	1.59	0.243
Two-Way Interaction	3	2.2813	0.76044	11.59	0.003
$P \times V$	1	0.7780	0.77802	11.86	0.009
$P \times F$	1	1.1486	1.14856	17.51	0.003
$V \times F$	1	0.3547	0.35475	5.41	0.049
Error	8	0.5248	0.06560		
Lack-of-Fit	5	0.5107	0.10214	21.72	0.015
Pure Error	3	0.0141	0.00470		
Total	17	18.7254			

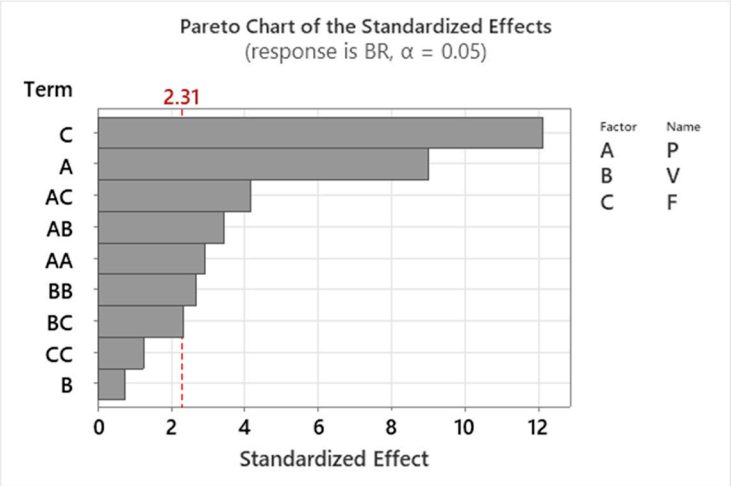

Figure 8. Pareto chart (significance level, α = 0.05) of the standardized effects of process parameters on BR.

3.1.4. Dilution

Dilution (*DL*) is defined as the percentage of depth of track (*D*) to the sum of depth and height as shown in Equation (7). It indicates the extent to which the substrate is melted during LDED-PF deposition. It is ideal to have dilution to a certain degree to have a good metallurgical bond between the deposit and substrate. However, a higher value of *DL* can result in an increase in the mixing zone and over-melting of the previous layer during multi-layer deposition. *DL* increases with an increase in LEL and a reduction in PFL as shown in Figure 9. The increase in *DL* with an increase in LEL is mainly due to the increase

in the amount of energy available to melt the substrate. On the other hand, with an increase in PFL, the amount of material available for absorbing the laser energy increases and the amount of laser energy impinging on the substrate is reduced, which results in a reduction in *DL*.

$$DL = \left(\frac{D}{D+H}\right) \times 100 \tag{7}$$

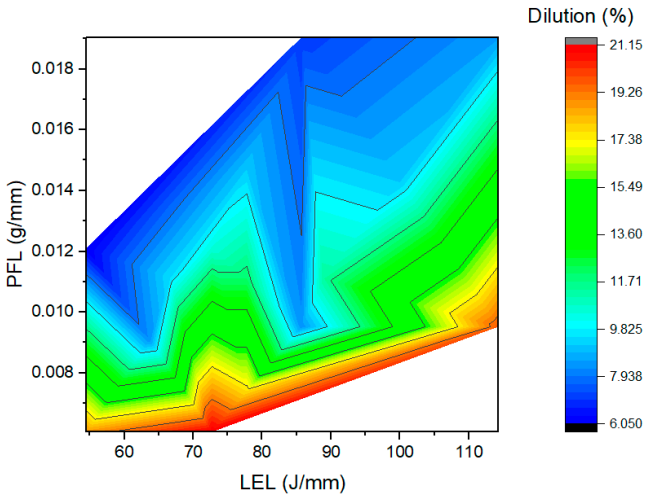

Figure 9. Effect of LEL and PFL on *DL*.

An ANOVA is performed to statistically examine the relative significance of the LDED-PF process parameters on *DL* as presented in Table 6. *F* is the most significant process parameter influencing *DL*, followed by *P* and *V*. The contributions of *F* and *P* towards *DL* are 56.9% and 13.2%, respectively. The Pareto chart presented in Figure 10 also shows that F is the most significant parameter in determining the *DL* of Fe20Cr5.5AlY deposits. The response model of *DL* is shown in Equation (8). The R^2 of 0.89 indicates a good correlation between the experimental values and predicted values and the model's significance is indicated by the *p* value < 0.05. It can be concluded that the model is significant with an 89.5% contribution towards explaining the behavior of *DL*.

$$\begin{aligned} DL = 71.5 + 0.094\,P + 13.20\,V - 4.34\,F - 0.000006\,P \times P - 0.438\,V \times V + 0.719\,F \times F - 0.00380\,P \times V \\ - 0.00488\,P \times F - 0.344\,V \times F \end{aligned} \tag{8}$$

Table 6. ANOVA analysis of dilution.

Source	DF	Adj SS	Adj MS	*F*-Value	*p*-Value
Model	9	310.460	34.496	7.62	0.004
Linear	3	257.661	85.887	18.96	0.001
P	1	46.094	46.094	10.18	0.013
V	1	14.341	14.341	3.17	0.113
F	1	197.227	197.227	43.54	0.000
Square	3	25.444	8.481	1.87	0.213
$P \times P$	1	0.011	0.011	0.00	0.962
$V \times V$	1	8.299	8.299	1.83	0.213
$F \times F$	1	22.423	22.423	4.95	0.057
Two-Way Interaction	3	27.355	9.118	2.01	0.191
$P \times V$	1	4.622	4.622	1.02	0.342
$P \times F$	1	7.607	7.607	1.68	0.231
$V \times F$	1	15.126	15.126	3.34	0.105
Error	8	36.239	4.530		
Lack-of-Fit	5	34.772	6.954	14.22	0.027
Pure Error	3	1.467	0.489		
Total	17	346.699			

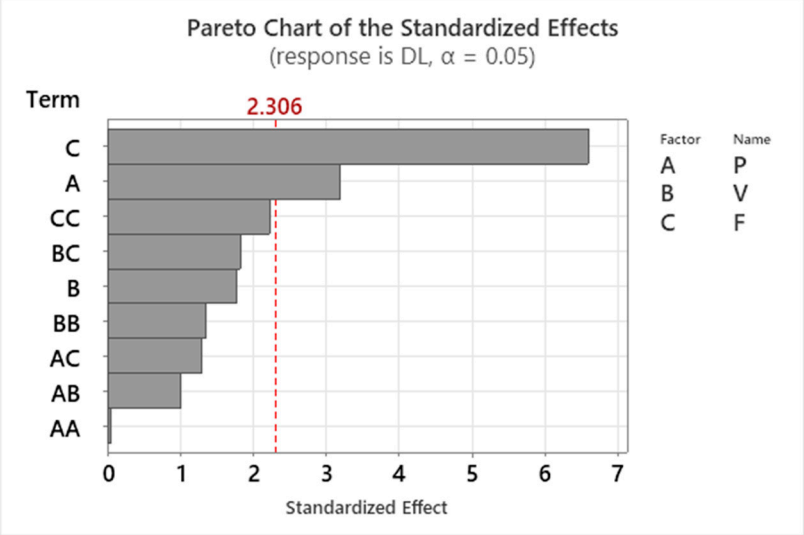

Figure 10. Pareto chart (significance level, $\alpha = 0.05$) of the standardized effects of process parameters on dilution.

3.2. Multi-Objective Optimization

The multi-objective optimization approach is used to establish the optimum solution, which is the best possible combination of LDED-PF process parameters which meets two objectives to achieve a maximum build rate and target dilution of 10%. One of the approaches to solving a multi-objective optimization problem is the use of a desirability function, which converts the values of the estimated responses into a free scale. Generally, the value ranges from 0 to 1, in which 0 and 1 indicate the unsatisfactory level and the target or acceptable limit, respectively [30]. According to the desirability plot in Figure 11 and the resulting optimum setting of parameters shown in Table 7, the most desirable operating conditions are P = 800 W, V = 10 mm/s, and F = 8 g/min with the desirability value of 0.94. Table 8 presents the comparison between the predicted values and actual measured values, which shows good agreement. Therefore, the established prediction models can accurately predict the geometric characteristics of single tracks adequately.

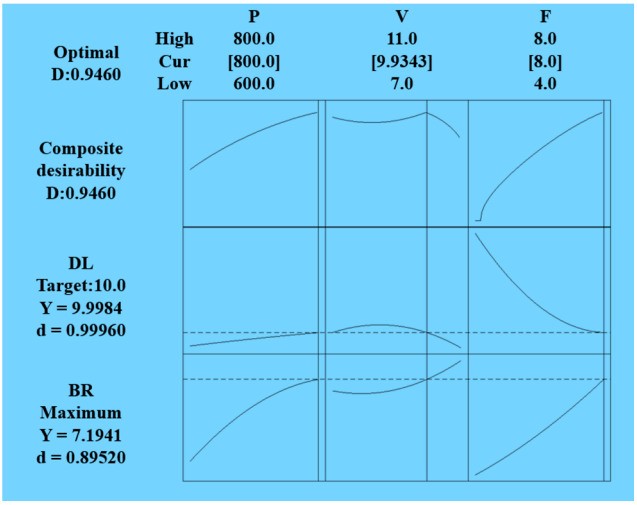

Figure 11. Desirability plot of *BR* and *DL*.

Table 7. Optimization results of the model.

Solution	*P*	*V*	*F*	*DL* Fit	*BR* Fit	Composite Desirability
1	800.000	9.9343	8.00000	9.9984	7.19410	0.945959
2	800.000	10.0016	7.98200	9.9133	7.20655	0.937121
3	800.000	10.0728	7.98913	9.8141	7.24508	0.929358
4	766.339	9.7252	8.00000	9.9824	6.95365	0.915554
5	799.675	7.0000	8.00000	10.0000	6.84436	0.904328

Table 8. Predicted and actual values under optimum process parameters.

Optimized Process Parameters			*BR* (mm^3/min)		*DL* (%)	
P	*V*	*F*	Predicted	Actual	Predicted	Actual
800	10	8	7.19	8.9	9.99	11

3.3. Multi-Track Deposition

Figure 12a,b presents the top view and 3D profile of the deposited clad layer, respectively. It can be seen that the clad layer is defect-free at the macroscale. The partially melted powders are observed on the surface of the clad layers, which is typically seen during the LDED-PF deposition. The waviness pattern on the surface is mainly due to the linear scanning strategy deployed for the study. Figure 12c presents the surface profile of the top layer of deposition along a central plane, which indicates a maximum surface deviation of 0.42 mm on the surface. Figure 12d presents the cross-section of the multi-track clad layer. The clad layer is largely defect-free in nature. It shows sound metallurgical bonding between the substrate and clad layer without any sign of delamination or defects in the fusion zone. The curvature of the fusion zone proves that substantial melting of the substrate material occurred. Micro-pores are seen at some locations, which are a mix of spherical and elongated pores. The spherical pores are gas pores that may be developed during laser cladding due to gas entrapment in the melt pool. In addition, as gas-atomized powders are used for deposition, the gas pores can also be due to pores trapped inside the powder particles during powder production. The irregular pores are due to a lack of complete fusion at some locations during the deposition.

The presence of irregularly shaped inclusions is observed occasionally in the as-deposited sample as labelled in Figure 12d. In order to understand the composition of these inclusions, an EDS analysis was performed on one of the isolated slag deposits (region 1) as shown in Figure 13a. Fe and Cr are absent at the inclusion, while the presence of Al, Y, and Zr at the inclusion is evident. This can be due to the formation of a complex oxide slag layer, which is formed during the deposition. Subsequent to the deposition, they are retained in the matrix of the alloy. The developed oxide slag layers can be a combination of $Y_3Al_5O_{12}$ (YAG), Al_2O_3, and ZrO_2, which are formed during LDED-PF. Similar observations are reported on oxide dispersion-strengthened (ODS) alloys built using LDED-PF [32]. In addition, it can also be noted from Figure 13a that the composition is uniform in the deposited layer (region 2). This is indicated by the uniform distribution of the elements along the grain and grain boundaries, which shows that there are no precipitation effects during LDED-PF of the alloy.

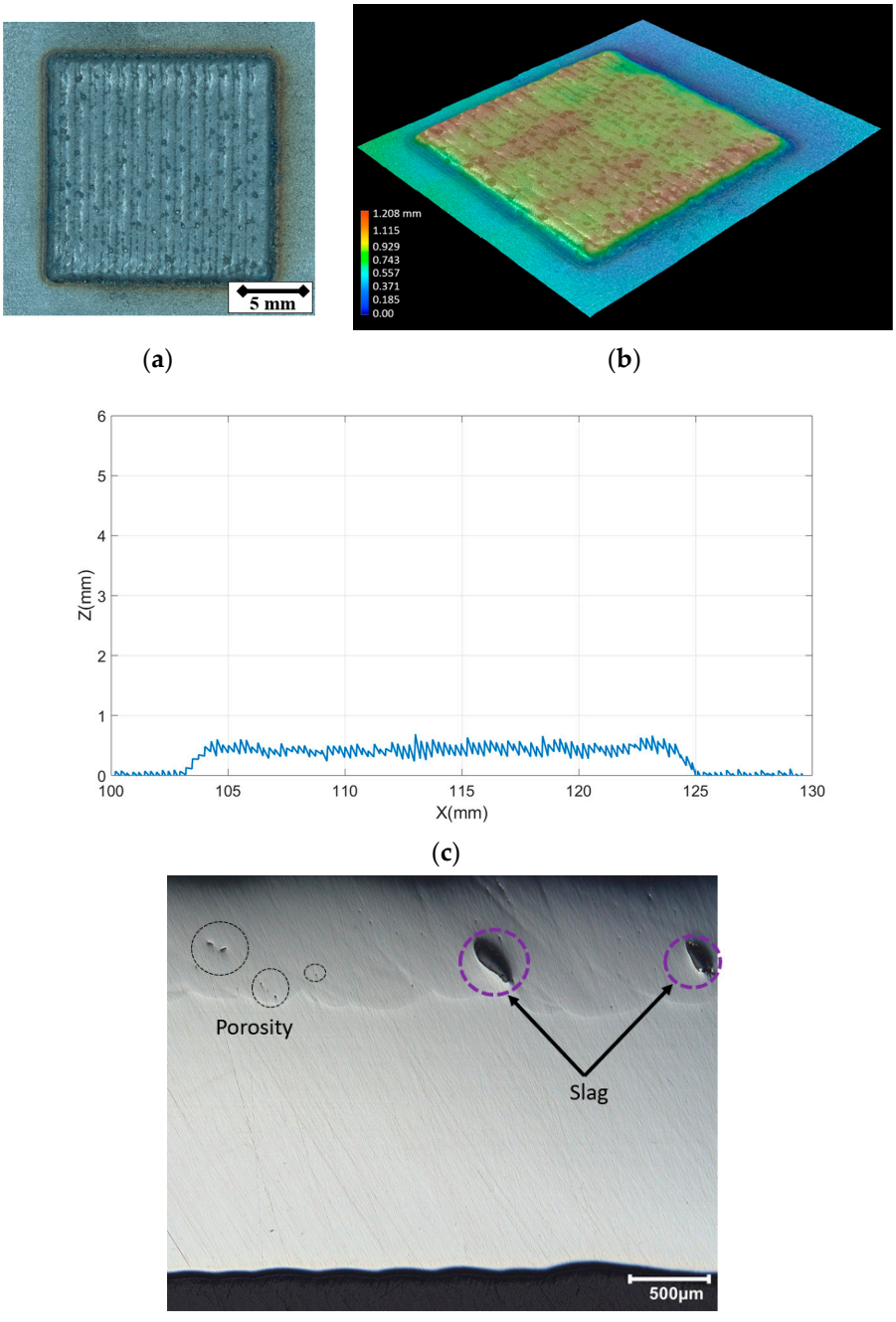

Figure 12. Multi-track clad layer: (**a**) photographic view, (**b**) 3D map, (**c**) geometry profile, (**d**) cross-section.

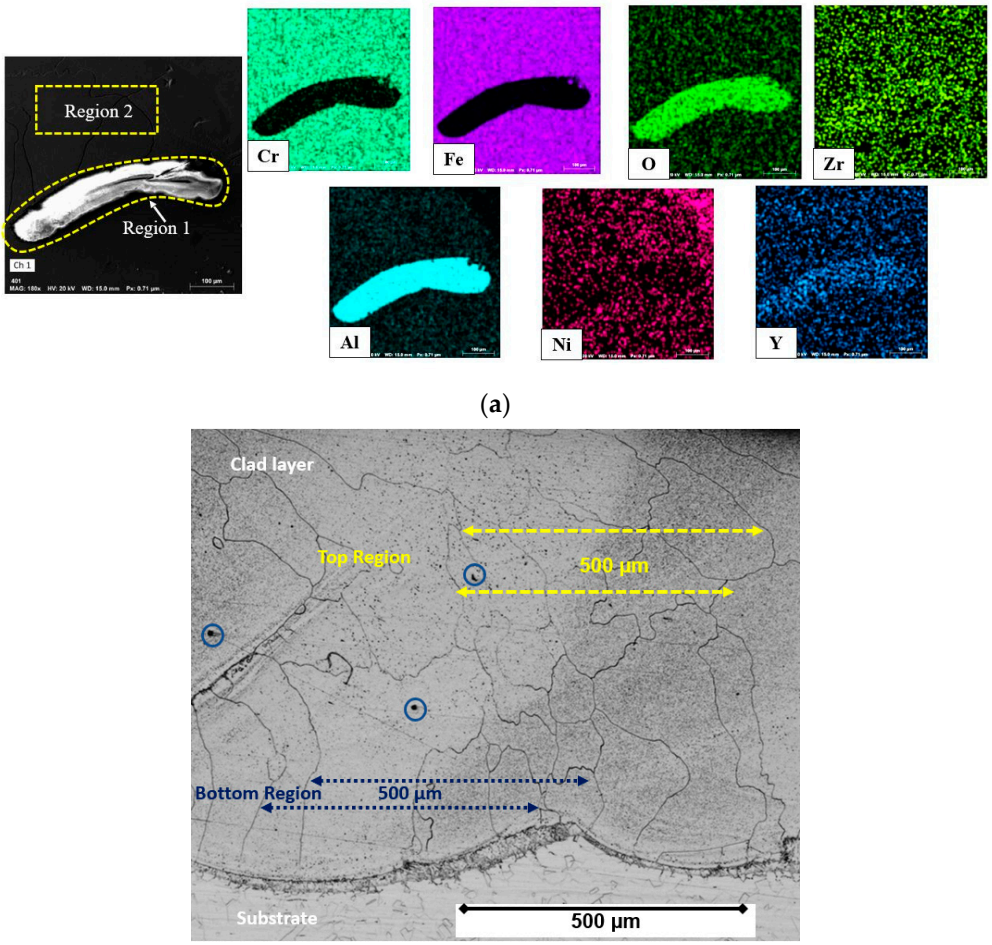

Figure 13. Cross-section analysis of the clad layer: (**a**) EDS mapping of slag, (**b**) microstructure.

The microstructure of the clad layer is presented in Figure 13b. The presence of elongated and spherical pores discussed previously can be seen with the ~15 µm size. The microstructure is primarily columnar in nature, which is mainly oriented parallel to the build direction. However, the inclination of the grain growth is evident along the cross-section, which is produced by the curvature of the melt pool. During the LDED-PF process, the powder was captured by the high-energy laser and a melt pool was formed. The heat flow was mainly dissipated from the melt pool to the substrate, which led to a high-temperature gradient. The grains prefer to grow opposite to the direction of heat transfer. It can also be seen that the average grain size is ~125 µm in the bottom zone of the clad, while the grain size is ~170–180 µm in the top region of the clad.

Micro-hardness measurements along the clad layer show the hardness ranges from 240 to 285 HV, with a hardness of ~225 HV at the substrate as shown in Figure 14a. A comparison with the literature shows that similar hardness values are observed for Fe–Cr–Al wire deposited using laser welding [33]. Hardness indentations are taken at the slag layer, and a microhardness in the range of 1088–1276 HV is observed. In addition, cracks are seen to originate from the tip of the indentation, indicating the brittle nature of the slag layer as seen in Figure 14b.

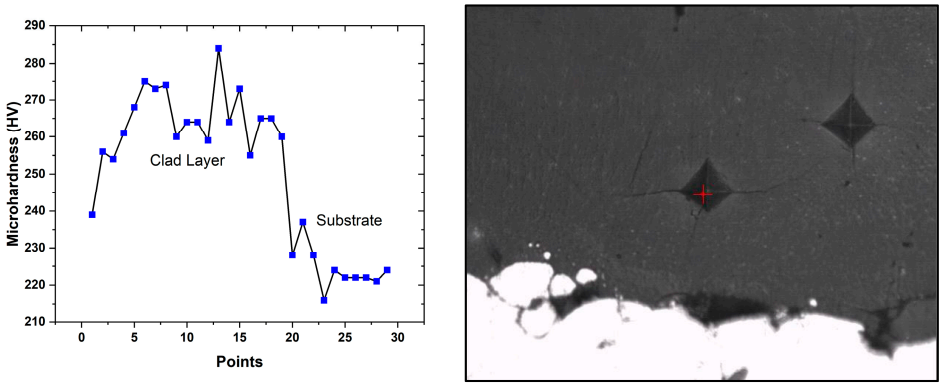

(**a**) (**b**)

Figure 14. Microhardness: (**a**) along the clad layer, (**b**) indentation at the slag layer.

3.4. Multi-Layer Deposition

Figure 15a presents the photographic view of 20 mm × 20 mm × 5 mm multi-layered Fe20Cr5.5AlY structures built using LDED-PF. The Archimedes density analysis indicates an average density of 7.08 g/cc with a relative density of 99.7%. The cross-sectional analysis of the bulk structures indicates that the deposition is majorly defect-free except for the presence of a few micro-pores (indicated with red circle) as seen in Figure 15b. The pores are a mix of circular and irregular pores, indicating the presence of gas porosities and a lack of fusion pores. The presence of a slag layer is observed in the multi-layered structures (as labelled in Figure 15b) similar to the multi-track clad layer. Details on the slag formation were explained earlier. The microstructural analysis shows the presence of columnar growth with an increase in the grain size as the deposition moves from the bottom layers to the top layers as seen in Figure 15c,d. The fine grain structure at the bottom layers can be due to the substrate effect which provides a larger thermal gradient and higher cooling rates. As the deposition moves from the bottom layer to the top layer, the heat accumulation may reduce the cooling rates and increase the grain size. Figure 15e presents the micro-hardness values of the multi-layered structures. The average micro-hardness is 243 HV, which is higher than the average microhardness reported for Kanthal® APM (225 HV) [28], which can be due to the fine grain structure typically observed in LDED-PF. The micro-hardness values obtained for multi-layered structures are lower than the single-layer deposition, which can be the effect of continuous thermal cycling and relatively lower cooling rates due to the preheating effect from the previous layer during multi-layer deposition.

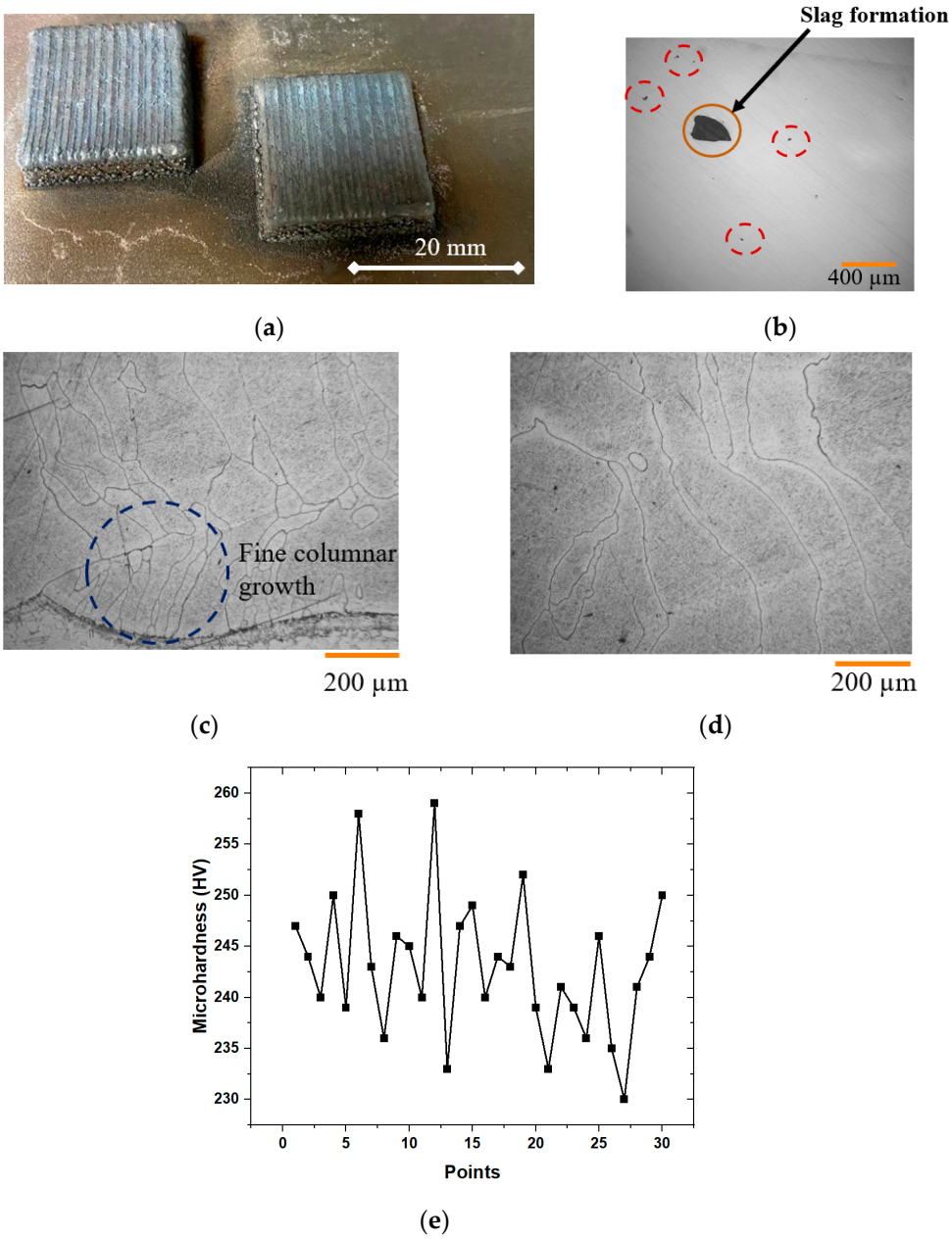

Figure 15. Multi-layer structures. (**a**) Photographic view; (**b**) Cross-section image; (**c**) Microstructure at the interface; (**d**) Microstructure at top layers; (**e**) Microhardness measurements.

4. Conclusions

The present work focused on the process development for LDED-PF of Fe20Cr5.5AlY, an alumina-forming steel from single-tracks to multi-tracks and multi-layer deposition. The following conclusions can be derived from the work:

- The single-track analysis shows that *W* and *H* are mainly governed by LEL and PFL, respectively. *P* contributes significantly to the *W*, while *V* and *F* mainly govern the *H*.
- *BR* and *DL* were considered for optimizing the process parameters. *BR* and *DL* are mainly dependent on the *F*, and the effect of *P* on the *BR* and *DL* is found to be more significant than that of *V*.
- The multi-objective optimization approach using the desirability function indicates that the most desirable operating conditions for maximum *BR* and desired *DL* are *P* = 800 W, *V* = 10 mm/s, and *F* = 8 g/min. The established prediction models were found to accurately predict the geometric characteristics of single tracks satisfactorily.

- The multi-track deposition yielded densely clad layers with the presence of few micro-pores. The microstructure was mainly columnar and the microhardness ranged from 240 to 285 HV. The presence of irregularly shaped inclusions was observed occasionally in the as-deposited sample, which was rich in the oxides of Al, Y, and Zr, with a hardness of 1088–1276 HV.
- The multi-layer deposition indicated a density of 99.7%, and the presence of micro-pores and slag layers were also observed. The columnar growth was finer at the bottom layers, with an increase in the grain size as the deposition moved to the top layer. The average micro-hardness of multi-layered bulk structures was 243 HV, which is higher than the average microhardness reported for commercially available Kanthal® APM.

The study paves the way towards the development of large-scale claddings and the fabrication of components using Fe20Cr5.5AlY for power generation applications. The study will be extended to the analysis of the bulk properties of depositions by evaluating adhesive properties at different temperatures.

Author Contributions: Conceptualization, J.A.N. and E.T.; methodology, J.A.N.; software, F.K.; formal analysis, J.A.N. and F.K.; investigation, J.A.N.; resources, M.Z. and E.T.; writing—J.A.N.; writing—review and editing, F.K., M.Z. and E.T.; supervision, E.T.; project administration, E.T. and M.Z.; funding acquisition, E.T. and M.Z. All authors have read and agreed to the published version of the manuscript.

Funding: This research was funded by the Federal development of Ontario (Fed-Dev) and Promation Engineering.

Data Availability Statement: Not applicable.

Conflicts of Interest: The authors declare no conflict of interest.

References

1. Reddy, L.; Sattari, M.; Davis, C.J.; Shipway, P.H.; Halvarsson, M.; Hussain, T. Influence of KCl and HCl on a Laser Clad FeCrAl Alloy: In-Situ SEM and Controlled Environment High Temperature Corrosion. *Corros. Sci.* **2019**, *158*, 108076. [CrossRef]
2. Bryers Livingston, R.W. Fireside Slagging, Fouling and High-Temperature Corrosion of Heat-Transfer Surface Due to Impurities in Steam-Raising Fuels. *Prog. Energy Combust. Sci.* **1996**, *22*, 29–120. [CrossRef]
3. Israelsson, N.; Unocic, K.A.; Hellström, K.; Jonsson, T.; Norell, M.; Svensson, J.-E.; Johansson, L.-G. A Microstructural and Kinetic Investigation of the KCl-Induced Corrosion of an FeCrAl Alloy at 600 °C. *Oxid. Met.* **2015**, *84*, 105–127. [CrossRef]
4. Tolpygo, V.K.; Viefhaus, H. Segregation at the Al_2O_3-FeCrAl Interface During High-Temperature Oxidation. *Oxid. Met.* **1999**, *52*, 1–29. [CrossRef]
5. Zhang, Z.L.; Li, D.Y.; Dong, X.Q. Microstructural Study of Fe-Cr-Al/Al Composite Coatings during Oxidation and Sulfidation at 900 °C. *Acta Metall. Sin. English Lett.* **2007**, *20*, 87–94. [CrossRef]
6. Gunduz, K.O.; Visibile, A.; Sattari, M.; Fedorova, I.; Saleem, S.; Stiller, K.; Halvarsson, M.; Froitzheim, J. The Effect of Additive Manufacturing on the Initial High Temperature Oxidation Properties of RE-Containing FeCrAl Alloys. *Corros. Sci.* **2021**, *188*, 109553. [CrossRef]
7. Nicholls, J.R.; Bennett, M.J.; Newton, R. A Life Prediction Model for the Chemical Failure of FeCrAlRE Alloys: Preliminary Assessment of Model Extension to Lower Temperatures. *Mater. High Temp.* **2003**, *20*, 429–438. [CrossRef]
8. Valiente Bermejo, M.A.; Magniez, L.; Jonasson, A.; Selin, S.; Frodigh, M.; Hurtig, K.; Stridh, L.E.; Karlsson, L. Exposure of FeCrAl Overlay Welds on Superheater Tubes: Influence of Local Environment on Degradation. *J. Fail. Anal. Prev.* **2022**, *22*, 400–408. [CrossRef]
9. Quadakkers, W.J.; Naumenko, D.; Wessel, E.; Kochubey, V.; Singheiser, L. Growth Rates of Alumina Scales on Fe–Cr–Al Alloys. *Oxid. Met.* **2004**, *61*, 17–37. [CrossRef]
10. Berthomé, G.; N'Dah, E.; Wouters, Y.; Galerie, A. Temperature Dependence of Metastable Alumina Formation during Thermal Oxidation of FeCrAl Foils. *Mater. Corros.* **2005**, *56*, 389–392. [CrossRef]
11. Josefsson, H.; Liu, F.; Svensson, J.-E.; Halvarsson, M.; Johansson, L.-G. Oxidation of FeCrAl Alloys at 500–900 °C in Dry O_2. *Mater. Corros.* **2005**, *56*, 801–805. [CrossRef]
12. Götlind, H.; Liu, F.; Svensson, J.-E.; Halvarsson, M.; Johansson, L.-G. The Effect of Water Vapor on the Initial Stages of Oxidation of the FeCrAl Alloy Kanthal AF at 900 °C. *Oxid. Met.* **2007**, *67*, 251–266. [CrossRef]
13. Ndumia, J.N.; Zhu, J.; Gbenontin, B.V.; Kang, M.; Liu, X.; Nyambura, S.M. Effect of Heat Treatment on the Microstructure and Corrosion Behavior of Arc-Sprayed FeCrAl/Al Coating. *J. Mater. Eng. Perform.* **2022**, 1–9. [CrossRef]

14. Wang, Y.; Zhou, W.; Wen, Q.; Ruan, X.; Luo, F.; Bai, G.; Qing, Y.; Zhu, D.; Huang, Z.; Zhang, Y.; et al. Behavior of Plasma Sprayed Cr Coatings and FeCrAl Coatings on Zr Fuel Cladding under Loss-of-Coolant Accident Conditions. *Surf. Coatings Technol.* **2018**, *344*, 141–148. [CrossRef]
15. Kim, I.H.; Jung, Y.I.; Kim, H.G.; Jang, J.I. Oxidation-resistant coating of FeCrAl on Zr-alloy tubes using 3D printing direct energy deposition. *Surf. Coatings Technol.* **2021**, *411*, 126915. [CrossRef]
16. Zhang, Y.; Lv, G.; Li, Y.; Tang, Z.; Nie, Z. The Design of Reflected Laser Intensity Testing System and Application of Quality Inspection for Laser Cladding Process. *Machines* **2022**, *10*, 821. [CrossRef]
17. Dai, Q.; Liu, L.; You, F.; Luo, C. Grinding Performance of Laser Cladding WC/Fe Coatings by Different Adding Methods of WC Particles. *Machines* **2022**, *10*, 910. [CrossRef]
18. Toyserkani, E.; Sarker, D.; Ibhadode, O.O.; Liravi, F.; Russo, P. *Metal Additive Manufacturing*, 1st ed.; Wiley: New York, NY, USA, 2021.
19. Jinoop, A.N.; Paul, C.P.; Bindra, K.S. Laser-Assisted Directed Energy Deposition of Nickel Super Alloys: A Review. *Proc. Inst. Mech. Eng. Part L J. Mater. Des. Appl.* **2019**, *233*, 2376–2400. [CrossRef]
20. Ahn, D.-G. Directed Energy Deposition (DED) Process: State of the Art. *Int. J. Precis. Eng. Manuf. Technol.* **2021**, *8*, 703–742. [CrossRef]
21. Liu, C.A.; Humphries, M.J.; Krutenat, R.C. Production of Fe-Cr-Al-Y and Co-Cr-Al-Y Coatings by Laser Surface Fusion and Their Oxidation Behavior. *Thin Solid Films* **1983**, *107*, 269–275. [CrossRef]
22. Nagarathnam, K.; Komvopoulos, K. Microstructural Analysis and Oxidation Behavior of Laser-Processed Fe-Cr-AI-Y Alloy Coatings. *Metall. Mater. Trans. A* **1996**, *27*, 381–390. [CrossRef]
23. Yang, Y.; Li, Y.; Liang, Z.; Bai, P.; Nie, J.; Liu, S.; Chen, B.; Wei, S.; Guan, Q.; Cai, J. Continuous Hot Corrosion Behaviour of an FeCrAlSi Coating Prepared by Laser Cladding. *Surf. Coatings Technol.* **2021**, *421*, 127424. [CrossRef]
24. Kaji, F.; Jinoop, A.N.; Zimny, M.; Frikel, G.; Tam, K.; Toyserkani, E. Process Planning for Additive Manufacturing of Geometries with Variable Overhang Angles Using a Robotic Laser Directed Energy Deposition System. *Addit. Manuf. Lett.* **2022**, *2*, 100035. [CrossRef]
25. Kaji, F.; Nguyen-Huu, H.; Budhwani, A.; Narayanan, J.A.; Zimny, M.; Toyserkani, E. A Deep-Learning-Based in-Situ Surface Anomaly Detection Methodology for Laser Directed Energy Deposition via Powder Feeding. *J. Manuf. Process.* **2022**, *81*, 624–637. [CrossRef]
26. Guo, C.; He, S.; Yue, H.; Li, Q.; Hao, G. Prediction Modelling and Process Optimization for Forming Multi-Layer Cladding Structures with Laser Directed Energy Deposition. *Opt. Laser Technol.* **2021**, *134*, 106607. [CrossRef]
27. Lian, G.; Yao, M.; Zhang, Y.; Chen, C. Analysis and Prediction on Geometric Characteristics of Multi-Track Overlapping Laser Cladding. *Int. J. Adv. Manuf. Technol.* **2018**, *97*, 2397–2407. [CrossRef]
28. KANTHAL® APM. Available online: https://www.kanthal.com/en/products/material-datasheets/tube/kanthal-apm/ (accessed on 6 October 2022).
29. Kao, A.; Gan, T.; Tonry, C.; Krastins, I.; Pericleous, K. Thermoelectric Magnetohydrodynamic Control of Melt Pool Dynamics and Microstructure Evolution in Additive Manufacturing. *Philos. Trans. R. Soc. A Math. Phys. Eng. Sci.* **2020**, *378*, 20190249. [CrossRef]
30. Le, T.-N.; Lo, Y.-L. Effects of Sulfur Concentration and Marangoni Convection on Melt-Pool Formation in Transition Mode of Selective Laser Melting Process. *Mater. Des.* **2019**, *179*, 107866. [CrossRef]
31. Ali, M.A.; Ishfaq, K.; Jawad, M. Evaluation of Surface Quality and Mechanical Properties of Squeeze Casted AA2026 Aluminum Alloy Using Response Surface Methodology. *Int. J. Adv. Manuf. Technol.* **2019**, *103*, 4041–4054. [CrossRef]
32. Shi, Y.; Lu, Z.; Yu, L.; Xie, R.; Ren, Y.; Yang, G. Microstructure and Tensile Properties of Zr-Containing ODS-FeCrAl Alloy Fabricated by Laser Additive Manufacturing. *Mater. Sci. Eng. A* **2020**, *774*, 138937. [CrossRef]
33. Yang, S.; Xi, B.; Zhang, Y.; Wang, D.; Liu, B.; Szakálos, P.; Ejenstam, J.; Wallenius, J.; He, G.; Zhang, W. Development of a Welding Process to Overlay FeCrAl Alloy on a Thin Wall Austenitic Stainless Steel Tube. *Nucl. Mater. Energy* **2021**, *27*, 100958. [CrossRef]